

# Experimental and Numerical Simulations of Spray Impingement and Combustion Characteristics in Gasoline Direct Injection Engines under Variable Driving Conditions

Juhyeong Seo<sup>1</sup> · Ho Young Kim<sup>1</sup>  · Simsoo Park<sup>1</sup> · Scott C. James<sup>2</sup> · Sam S. Yoon<sup>1</sup>

Received: 15 March 2015 / Accepted: 25 October 2015 / Published online: 11 November 2015  
© Springer Science+Business Media Dordrecht 2015

**Abstract** Gasoline direct injection (GDI) increases engine power output and reduces emissions. In GDI engines, increasing injection pressure improves atomization, which increases thermal efficiency at the cost of wall wetting. When wall wetting occurs, both soot emissions and fuel consumption increase. Wall wetting in GDI engines under cold driving conditions has rarely been considered. In this study, experimental data characterizing droplet splashing/spreading phenomena were collected to inform numerical simulations of combustion characteristics and wall wetting subject to variable driving conditions and excess air ratio,  $\lambda$ . Fully 3D and unsteady numerical simulations were carried out to predict flow-field, combustion, and spray-impingement characteristics. To simulate a GDI engine, a spray-impingement model was developed using both experimental data and previous modeling efforts. The excess air ratio and driving-condition temperature were the variable parameters considered in this study. When decreasing  $\lambda$  from 1.0 to 0.7 by increasing the fuel-injection rate (fuel rich), the cylinder pressure increases to 61 % of the pressure when  $\lambda = 1.0$ . Because of increasing the fuel-injection rate, the increased momentum in the fuel spray increases both wall wetting and soot generation. At low driving-condition temperatures, the cylinder pressure was up to 63 % less than that under warm conditions, but with increased soot generation. Simulations revealed a correlation between wall wetting and the soot emissions. Soot generation was most sensitive to changes in wall wetting.

**Keywords** Spray-wall impingement · Direct injection · Gasoline engine · Wall wetting

---

✉ Ho Young Kim  
kimhy@korea.ac.kr

<sup>1</sup> School of Mechanical Engineering, Korea University, Seoul, Korea

<sup>2</sup> Departments of Geology and Mechanical Engineering, Baylor University, Waco, TX 76798, USA

## 1 Introduction

Direct injection is a state-of-the-art technology in the automotive industry that increases power output, fuel economy, and the compression ratio of an engine [1–4]. High-pressure direct injection improves fuel atomization [5]; however, it also increases the momentum of the spray, which allows fuel droplets to traverse the combustion chamber and impinge upon the piston surface or cylinder walls [6].

When wall wetting occurs, particulate matter (PM) emissions form during the combustion process [7–9]. Studies have shown that wall wetting decreases the fuel evaporation rate, which impairs fuel economy [10]. Under warmed-up operating conditions, the combustion-chamber temperature is sufficiently high to evaporate nearly all of the fuel such that little, if any, impinges upon the walls before ignition [11]. In addition, more fuel is required under cold operating conditions to yield an equivalent combustion energy because additional heat is required to evaporate all of the fuel. This negative feedback loop increases the fuel-injection rate leading to more wall wetting, which increases the amount of unburned hydrocarbons. Much of the total PM emissions occur under cold operating conditions [12, 13]; reducing the amount of wall wetting under cold operating conditions is one of the easiest ways to minimize soot [14].

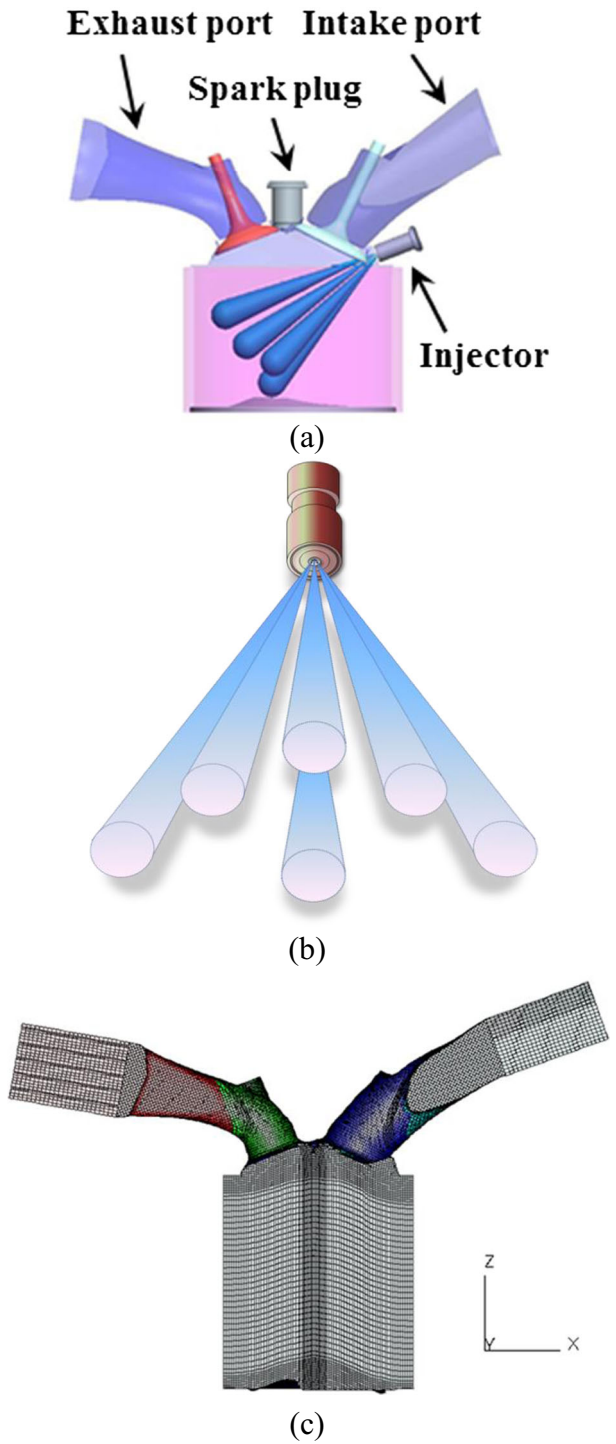
Several studies have shown that wall wetting can be reduced by optimizing the split-injection strategy or by varying the piston geometry [15–17]. However, spray impingement and the amount of wall wetting in real engines are difficult to observe and measure because these phenomena occur inside the combustion chamber. Laser-induced fluorescence techniques with an optical engine are used to measure wall wetting, but experiments are difficult to perform under cold operating conditions [18] or are limited to low-load conditions [19, 20]. Numerical simulations provide an alternative means for investigating wall wetting, but require accurate spray impingement models. In most numerical studies related to wall wetting, combustion was not considered; only spray impingement results were obtained [21–23].

In this study, the objectives were to experimentally and numerically investigate the combustion and spray impingement characteristics under variable driving conditions in a gasoline direct injection (GDI) engine with focuses on wall-wetting phenomena and optimizing fuel–air ratios to increase engine performance. Prior to the engine combustion simulation, a spray-impingement model for gasoline droplets was built. An experimental study on droplet impingement was used to identify regime-transition criteria and to characterize post-impingement features when developing the spray-impingement model. The numerical results were then verified by comparison to experimental data. The adjustable parameters were the ambient (operating) temperature (273, 294, and 410 K) and excess air ratio ( $\lambda = 0.7, 0.8, 0.9, \text{ and } 1.0$ ).

## 2 Target Engine Characteristics

The experiments and models were designed to represent a 2.4-L, naturally aspirated, four-stroke GDI engine with side fuel injection. The engine operating conditions were 1500 rpm with a brake mean effective pressure (BMEP) of 1.5 bar. Figure 1a is a schematic of the test engine. The start of injection/end of injection (SOI/EOI) and spark advance were before top dead center  $301^\circ/294^\circ$  CA bTDC and bTDC  $50^\circ$  CA, respectively. The solenoid-type injector has six holes (Fig. 1b) and was mounted on the side of the cylinder below

**Fig. 1** Schematics of the **a** test engine and **b** fuel-injection spray pattern as well as **c** the computational mesh of the test engine at BDC. Half of a single-cylinder engine is shown



the intake port. The fuel plume forms from the six solid-cone spray patterns issuing from the 240  $\mu\text{m}$  injector holes. A camshaft-driven high-pressure pump was used to pressurize the injected fuel up to a maximum of 150 bar. The fuel spray Sauter mean diameter (SMD) was less than 22  $\mu\text{m}$  at 150 bar while the spray cone angle was 35°–80°. The excess-air ratio was nominally  $\lambda = 1$  (but was also adjusted in the numerical simulations) The intake and exhaust pressures were measured with a manifold air pressure (MAP) sensor and an exhaust pressure sensor, respectively. K-type thermocouples were used to measure temperatures from the intake and the exhaust. Each value was measured for approximately 60 s and averaged. Table 1 presents the engine specifications and operating conditions.

### 3 Numerical Description

A computational fluid dynamics simulation was implemented with the commercial code STAR-CD, version 4.20. The mesh was generated using the polyhedral trimming method using ES-ICE [24]. The included pre-/post-processor and solver were pro-STAR and STAR, respectively. The current mesh was generated by a method called trimming method [24]. The spray-impingement model was implemented through a user-defined function. The governing equations were discretized using the finite volume method. The pressure implicit with splitting of operators (PISO) algorithm was used [25]. The monotone advection and reconstruction scheme was applied, which is a second-order differencing scheme for spatial

**Table 1** Specifications of the target engine

Engine specification	
Engine type	In-line, Stoichiometric GDI
Fuel injection guidance type	Wall guided
Number of cylinders	4
Displacement [cc]	2359
Bore [mm]	88
Stroke [mm]	97
Compression ratio	11.3
Fuel injection pressure	Max. 150 bar
Operating conditions	
Engine speed [rpm]	1500
BMEP [bar]	1.5
Intake pressure [bar]	0.28
Exhaust pressure [bar]	1.01
SOI/EOI [bTDC]	301°/294° CA
Ignition timing [bTDC]	30° CA
IVO/IVC	−7°/67° CA
EVO/EVC	13°/31° CA
Intake valve lift [mm]	9.6
Exhaust valve lift [mm]	8.2
Octane number	92

discretization [26]. A fully implicit, second-order Euler scheme was adopted for temporal discretization.

The computational domain used to simulate the experimental engine, governing equations, and models that were adopted in this study are described below.

### 3.1 Computational domain of the test engine

To investigate the spray impingement and combustion characteristics of a GDI engine, a single-cylinder engine was used. Figure 1c shows the present 3D computational domain. For computational efficiency, half of the single-cylinder engine was considered including half the intake and exhaust ports (corresponding to Fig. 1a). To capture engine dynamics, a moving mesh was used to simulate the piston, cylinder walls, and valves. The number of cells varied from 195,000 nodes at top dead center (TDC) to 375,000 nodes at BDC. The minimum and maximum cell volumes were 0.51 and 1.91 mm<sup>3</sup>, respectively. A total of 15,000 fuel parcels was selected to adequately represent the spray droplets forming the fuel plume for each fuel injection. The initial droplet diameter was set to the size of the injector hole (240 μm). The operating time step was 0.1° CA, which corresponded to 1.11 × 10<sup>-5</sup> s. The grid sensitivity and time step dependency were investigated and selected appropriately.

### 3.2 Governing equations

A multi-phase flow system forms when fuel is injected into the combustion chamber and this two-phase system simulated using an Eulerian–Lagrangian approach. As is common, the governing equations in the continuous phase conserve mass, momentum, energy, and species [24].

For the dispersed phase, the mass, momentum, and energy equations are expressed as:

$$\frac{dm_d}{dt} = -2\pi \frac{\lambda}{c_p} D_d \left( 1 + 0.23Re^{0.5} \right) \ln \left[ 1 + \frac{c_p (T - T_d)}{h_{fg}} \right], \tag{1}$$

$$m_d \frac{du_d}{dt} = \frac{1}{2} C_D \rho A_d |u_i - u_d| (u_i - u_d) - V_d \nabla p - C_{am} \rho V_d \frac{d(u_d - u)}{dt} + m_d [g - \omega \times (\omega \times r) - 2(\omega \times u_d)], \tag{2}$$

$$m_d c_{p,d} \frac{dT_d}{dt} = -A_S q_d'' + h_{fg} \frac{dm_d}{dt}, \tag{3}$$

where  $\lambda D$ ,  $A$ ,  $V$ ,  $p$ ,  $g$ ,  $\omega$ , and  $r$  are the thermal conductivity, droplet diameter, droplet cross-section area, droplet volume, pressure, gravity acceleration, angular velocity, and distance vector, respectively. Variables and constants  $m_d$ ,  $c_p$ ,  $C_D$ ,  $A_S$ ,  $h_{fg}$ , and  $q_d''$  describe the mass of a single droplet, fuel specific heat, drag coefficient, droplet surface area, fuel latent heat of vaporization, and surface heat flux, respectively. The subscript  $d$  denotes the droplet. The mass equation is attributed to Kuo [27]. The momentum equation is based on the forces acting on the dispersed phase. The forces on the right-hand-side of Eq. 2 correspond to the drag force, pressure force, virtual mass force, and body force, respectively. The droplet temperature was determined from the heat balance, while the surface heat flux was obtained according to the procedure of El Wakil et al. [28].

A dynamic film model [29] was adopted for the wall-film governing equations; the interface between the gas and wall film was also considered [30]. Wall-film stripping is described by Friedrich et al. [31], and the droplet diameter from the wall-film was obtained according

to Maroteaux et al. [32]. The post-impingement characteristics are described below. The wall-film governing equations involve mass, momentum, energy, and species transport:

$$\frac{\partial}{\partial t} (\rho_{lq}) + \nabla \cdot (\rho_{lq} u_{lq}) = \frac{\dot{m}_{imp}}{h}, \quad (4)$$

$$\frac{\partial}{\partial t} (\rho_{lq} u_{lq}) + \nabla \cdot (\rho_{lq} u_{lq} u_{lq}) = -\nabla P_{lq} + \rho_{lq} g + \nabla \cdot \tau_{lq} + S_{imp} \delta (\xi - h), \quad (5)$$

$$\frac{\partial}{\partial t} (\rho_{lq} h_{lq}) + \nabla \cdot (\rho_{lq} u_{lq} h_{lq}) = \nabla \cdot (k_{lq} \nabla T_{lq}) + \frac{\dot{Q}_{imp}}{h}, \quad (6)$$

$$\frac{\partial}{\partial t} (\rho_{lq} Y_{lq}) + \nabla \cdot (\rho_{lq} u_{lq} Y_{lq}) = \nabla \cdot (D_{lq} \nabla Y_{lq}) + \frac{\dot{m}_{imp}}{h}, \quad (7)$$

where the subscripts  $lq$  and  $imp$  indicate wall wetting and droplet impingement, respectively. The symbols  $h$ ,  $k$ ,  $D$ , and  $\xi$  represent the wall-wetting thickness, thermal conductivity, mass-diffusion coefficient, and local coordinate normal to the wall with the positive direction toward the wall, respectively. The variables  $\dot{m}_{imp}$ ,  $S_{imp}$ , and  $\dot{Q}_{imp}$  represent the mass source per unit area due to the droplet sticking/separation, momentum source, and enthalpy source, respectively. Note that the mass diffusion coefficient ( $D = \nu/Sc = \mu\rho/Sc$ ) is defined as the kinetic viscosity,  $\nu$ , divided by the Schmidt number,  $Sc$ .

### 3.3 Numerical models

The renormalization group  $k-\varepsilon$  model was used to represent turbulence [33] in the Reynolds-averaged Navier–Stokes equations. Fuel was atomized upon injection. The Reitz and Diwakar model [34] simulates primary and secondary droplet breakups. Droplet separation, bounce, or fusion occur when they collide during fuel injection. The O'Rourke model was adopted for droplet interactions [35]. Combustion was simulated with the three-zone extended coherent-flame (ECFM-3Z) model [36]. The ECFM-3Z model comprises three stages to describe combustion: mixing, flame propagation, and post-flame with emissions. Each computational cell was apportioned into pure-fuel, pure-air plus exhaust gas recirculation (EGR), and mixed-gases zones. The mixed-gases zone is where the air and fuel mix and is where combustion occurs. Flame propagation is based on a flame surface density equation from Colin et al. [37]. The flame surface density equation involves the laminar flame speed [38] and the intermittent turbulent net flame stretch (ITNFS) model [39]. The turbulent flame speed was proposed by Fichot et al. [40]. The post-flame stage chemistry deals with the formation of several pollutants such as soot,  $\text{NO}_x$ ,  $\text{CO}/\text{CO}_2$ , and radicals (O, H, and OH). The selected soot model was based on the work of Mauss et al. [41]. The proposed  $\text{NO}_x$  formation model uses the extended Zeldovich mechanism. See the work of Colin et al. [36] for details on the equilibrium reactions and CO kinetic oxidation chemistry. Isooctane ( $\text{C}_8\text{H}_{18}$ ) was used in the simulation to represent gasoline [22, 42–44] and the octane number was changed to 92 to predict the knock phenomenon more accurately.

## 4 Results and Discussion

### 4.1 Spray impingement modeling

In this study, the accuracy of the spray-impingement modeling was verified using three techniques: (1) transition criteria were established to determine whether impinging droplets were deposited, rebounded, or splashed, (2) post-impingement characteristics for the

rebounding and splashing droplets were ascertained; and (3) the spray-impingement model was matched to experimental data.

#### 4.1.1 Droplet impingement experimental setup

Impingement experiments were performed to determine transition criteria between depositing, rebounding, and splashing droplets. Figure 2 is a schematic of the droplet impingement experimental setup. The experiment was conducted to identify the regime transition criteria from splash to rebound. Droplets were ejected through a stainless steel needle (EFD, 18-gauge, with an inner diameter of 0.84 mm and outer diameter of 1.27 mm). A syringe pump (KSD 100) supplied the test liquid: either gasoline or isooctane. The properties of gasoline (from a gas station) and isooctane (Sigma-Aldrich, purity: 99.0 %) are listed in Table 2. The density, viscosity, and surface tension were measured with a density cup (50 ml, Soltec), viscometer (LVDV-I + CP, Brookfield), and tensiometer (DCAT-11, Dataphysics), respectively. The freefall droplet impact velocity was varied from 0.37 to 4.04 m/s by varying the release height from 10 to 1200 mm (distance between the nozzle tip and substrate). In real engines, the velocity of the injected droplets may be reduced by the intake air and resident gas. Based on experimental results for spray in an engine, the average droplet velocity prior to wall impact was 32.14 m/s, but the piston speed was 4.85 m/s yielding a relative droplet-to-wall velocity of 27.29 m/s. While GDI spray speeds are much greater than those in this experiment, experimental velocities were selected to ensure droplet splashing, which must occur to determine the transition criteria. Droplets impinged upon an aluminum substrate with an average surface roughness of  $0.02 \mu\text{m}$ . Snapshots of droplet impingement were taken with a high-speed camera (Vision Research Inc., Phantom 7.3) equipped with  $1.56\text{-}\mu\text{m}/\text{pixel}$  zoom lenses. A recording rate of 18,000 fps captured the time evolution of droplet-impingement phenomena. A halogen lamp (250 W) was aligned with the camera for illumination. The camera was aimed at both oblique and side-views to observe droplet-impact behavior.

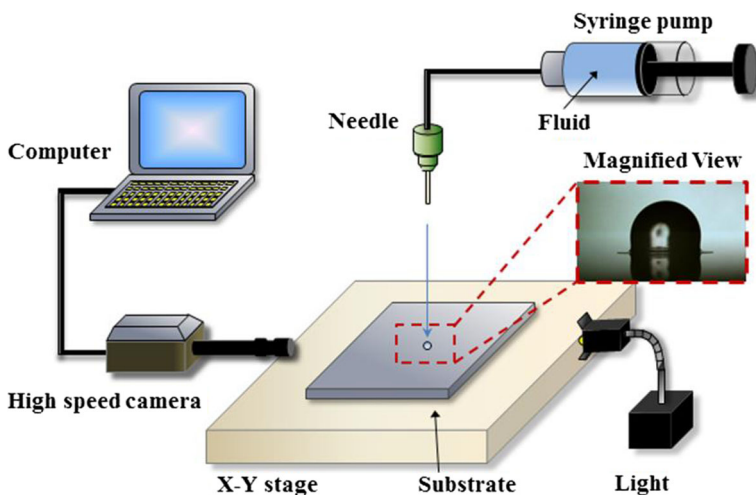


Fig. 2 Schematic of the droplet impingement experiments

**Table 2** Density, viscosity, and surface tension of gasoline and iso-octane with additional details for gasoline

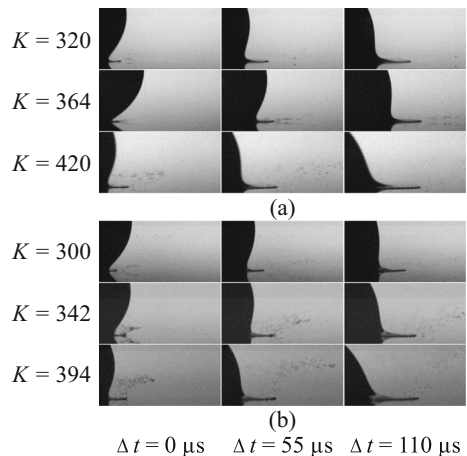
Liquid	Density [kg/m <sup>3</sup> ]	Viscosity [mPa·s]	Surface tension [mN/m]
Gasoline	706.4	0.46	18.21
Isooctane	684.2	0.55	18.06
Detailed properties of gasoline			
RON	93.2	Benzene [vol%]	0.49
Vapor pressure at 37.8°C [kPa]	70.9	Low heating value [J/g]	41,120
Density at 15°C [kg/m <sup>3</sup> ]	718	Distillation temperature [°C]	
Sulfur content [mg/kg]	5	10 vol%	49
Oxygen [wt%]	2.02	50 vol%	74
Aromatic [vol%]	15.7	90 vol%	144

#### 4.1.2 Results of droplet impingement

The experimentally determined transition criteria were used to distinguish the various impact modes of impinging droplets. These transition criteria are necessary for accurate numerical simulations and were determined for both gasoline and isooctane droplets. First, for both dry and wet substrates, the spread/splash transition criteria were established, followed by the rebound/spread transition criteria. Secondary droplets—defined as those ejected upon primary droplet impingement—were used to establish and distinguish the spread/splash transition criteria.

Figure 3 exemplifies how secondary droplets are ejected from primary gasoline and isooctane droplets upon impact. The velocities of the ejected secondary droplets for the gasoline and iso-octane droplets increased as the Weber ( $We = \rho DV^2/\sigma$ ) and Reynolds ( $Re = \rho DV/\mu$ ) number of the primary droplet increased. Both gasoline and isooctane demonstrated similar secondary droplet velocities. Compared to gasoline, isooctane

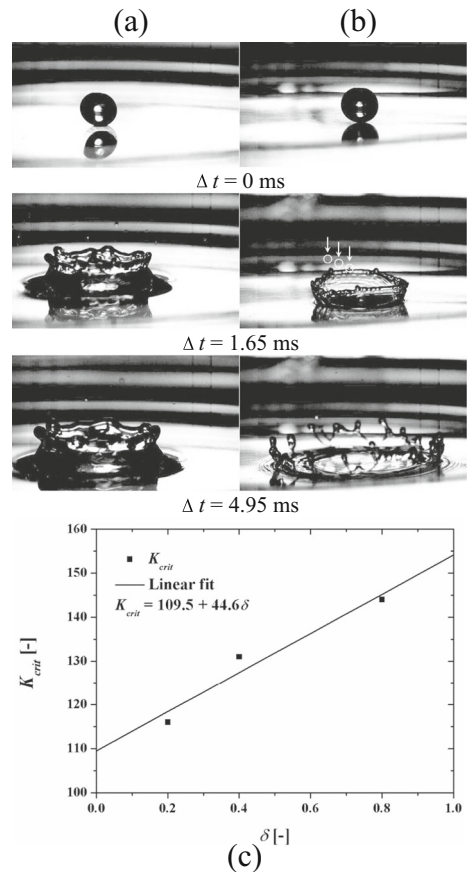
**Fig. 3** Magnified view of the secondary droplets splashed from **a** gasoline and **b** isooctane impinging upon a dry aluminum substrate



droplets splashed with a slightly larger secondary droplet inclination angle with no dominant variance. The spread/splash transition criteria were established based on the formation of secondary droplets, which indicates that splashing has occurred. The spread/splash transition criteria for wet-wall impingement are based upon the impingement parameter,  $K = We^{0.5}Re^{0.25}$ , as proposed by Mundo et al. [45]. The critical impingement parameters,  $K_{crit}$ , for gasoline and isoctane impinging upon a dry aluminum wall were both  $K_{dry,crit} \approx 233$ . For  $K > 233$ , splashing occurred upon impact. Figure 4 shows the results for an isoctane droplet impinging upon an isoctane film layer. The dimensionless film-layer thicknesses (layer thickness divided by the droplet diameter) were  $\delta = 0.2, 0.4,$  or  $0.8$ , as shown in Fig. 4c. Results indicated that the splash from a droplet impact occurred at a lower critical impingement parameter  $K_{crit}$  for thinner film layers. Values of  $K_{crit}$  for dimensionless film layer thicknesses of 0.2, 0.4, and 0.8, were  $K_{crit} = 116, 131,$  and  $144$ , respectively. The critical impingement parameter  $K_{w,crit}$  for the wet wall is estimated in Fig. 4c.

The rebound/spread transition criteria for both the dry and wet walls were also established. Similar to the spread/splash transition criteria, the rebound/spread transition criteria

**Fig. 4** Isoctane droplet splashes on a wetted film layer of dimensionless thicknesses: **a**  $\delta = 0.2$  and **b**  $\delta = 0.8$ . **c** Best-fit  $K_{crit}$  as a function of  $\delta$



were used to determine the transition from rebounding to spreading. The rebound/spread transition criterion for dry walls was based on the study by Rosa et al. [46], while the rebound/spread transition criterion for wet walls was established by combining the work of both Rosa et al. [46] and Stanton and Rutland [47]. Based on Rosa et al.’s work [21], the rebound/spread regime transition criterion for the dry wall is

$$K_{Rosa} < K_r = \begin{cases} 0 & T^* < 0 \\ K_1 [T^*]^\gamma & 0 < T^* < 1 \\ K_1 & 1 < T^* \end{cases}, \tag{8}$$

where  $K_r$  is the critical impingement parameter for distinguishing rebound and spread regimes. In Eq. 8,  $K_1 = 450$  and  $\gamma = 3$ , while  $K_{Rosa} = Oh^{-0.4}$  We and the dimensionless temperature is

$$T^* = \frac{T_{wall} - T_{boil}}{T_{leid} - T_{boil}}, \tag{9}$$

where subscripts *wall*, *boil*, and *leid* represent the wall, boiling, and Leidenfrost temperatures, respectively. Note that the Ohnesorge number is defined as  $Oh = We^{1/2}/Re$ . If  $K_{Rosa} < K_r$ , then the droplet rebounds from the wall.

For a wet wall, rebounding can occur even when the wall is below the boiling temperature. The Stanton and Rutland model [47] established the rebounding criterion below the boiling temperature. Accordingly, Eq. 8 can be modified as:

$$5 < We < 10 \quad T^* < 0 \\ K_{Rosa} < K_r = \begin{cases} K_1 [T^*]^\gamma & 0 < T^* < 1 \\ K_1 & 1 < T^* \end{cases} \tag{10}$$

Next, the post-impingement droplet characteristics were sought. For splashing droplets, post-impingement characteristics such as the mass ratio, secondary droplet diameter, and secondary droplet velocity were obtained. Note that the mass ratio is defined as a function of the primary-to-secondary droplet-size ratio. The mass ratio for a dry wall was taken from Grover and Assanis [48], while the mass ratio for a wet wall was derived from Bai and Gosman [49]. The mass ratio from Grover and Assanis [48] was estimated using the experimental data from Yarin and Weiss [50] and correlated to the experimental data of Stow and Stainer [51]. The mass ratio for the wet wall from Bai and Gosman [51] was based on the experimental study of Mutchler [52]. The mass ratio varies according to Weber number and whether the wall is wet or dry as follows:

$$\frac{m_s}{m_{imp}} = \begin{cases} 0.5, & We_{crit} < We < 600, & \text{dry wall} \\ 0.75, & We > 600, & \text{dry wall} \\ 0.2 + 0.9\alpha, & & \text{wet wall} \end{cases}, \tag{11}$$

where  $\alpha$  is a random selection from the standard uniform distribution. The subscripts *s* and *imp* represent secondary (splashed) and primary droplets, respectively. Secondary droplet conserve mass:

$$N_1 d_1^3 + N_2 d_2^3 = \frac{m_s}{m_{imp}} d^3, \tag{12}$$

where  $N$  and  $d$  are the number and diameter, respectively, of the secondary droplets. The total number of secondary droplets is [53]:

$$N_s = 0.1 Re_1; \quad Re_1 = \frac{U}{2\sqrt{\mu/\rho}} \left( \frac{\pi^2 \rho d^3}{\sigma} \right)^{1/4}. \tag{13}$$

Yoon and DesJardin [54] investigated the total number of secondary droplets using several models based on linear theories [55–57] and an empirical formula [53]. They concluded that Marmanis and Thoroddsen’s model [53] best predicts the total number of secondary droplets.

Two masses (or volumes) of secondary droplets were assumed. The two secondary droplet numbers were  $N_1$  and  $N_2$ . This assumption was made to derive the secondary droplet velocity of the splashing droplets, which was determined through conservation mass (12), momentum (15), and energy (16). After  $N_s$  was determined, the value of  $N_2$  was randomly selected from 1 to  $N_s - N_1$  because

$$N_1 + N_2 = N_s. \tag{14}$$

The secondary-droplet velocity was derived based on three equations for energy conservation, tangential momentum conservation, and size-velocity correlation of secondary droplets [58]. These are, respectively:

$$\frac{m_s}{2} u_1 \cos \theta_1 + \frac{m_s}{2} u_2 \cos \theta_2 = c_f m_{imp} u_{imp} \cos \theta_{imp}, \tag{15}$$

$$\frac{1}{4} m_s (u_1^2 + u_2^2) + \pi \sigma (N_1 d_1^2 + N_2 d_2^2) = E_k - E_{k,c}, \tag{16}$$

$$\frac{u_1}{u_i} \approx \ln \left( \frac{d_1}{d_i} \right). \tag{17}$$

The wall-friction coefficient is  $c_f = 0.5$  as suggested by Montanaro et al. [59]; Bai and Gosman [49] suggested a wall-friction coefficient between 0.6 and 0.8. Montanaro et al. [61] performed a spray impingement and compared it with a simulation using Bai and Gosman’s [49] model. The results showed that Bai and Gosman [49] overestimated the secondary droplet momentum for gasoline. The secondary droplet momentum carried a greater tangential velocity that resulted in secondary droplets splashes with higher velocities than expected. The ejection angle of the secondary droplet  $\theta_2$  was randomly selected between 5° and 50° [51].

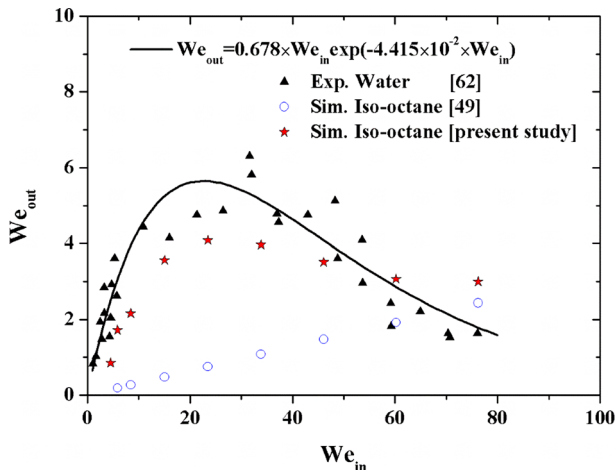


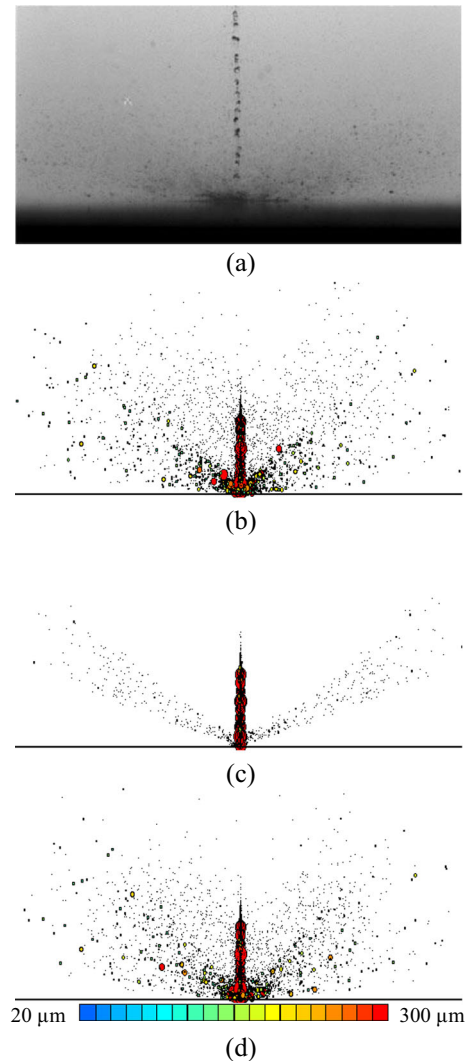
Fig. 5 Weber number of rebounding droplets before (in) and after impingement (out)

The post-impingement characteristics for rebounding droplets were derived through energy conservation. Each energy-conservation term for a rebounding droplet was in agreement with the study of Ryu [60], who measured their kinetic energy with droplet rebound velocities calculated as:

$$E_{S,2} + W_{rebound} = E_{S,3} + E_{KE,3}, \quad (18)$$

where subscripts  $S$ ,  $rebound$ , and  $KE$  represent the droplet surface energy, the work required for the droplet to rebound, and kinetic energy, respectively. Subscripted numbers represent the droplet state: the impinging droplet maximally spreads in state 2, and the droplet rebounds in state 3.

**Fig. 6** Comparisons between the spray impingement characteristics of **a** the experimental spray (taken by Powell and Lee [65] and reprinted in the study by Yoon and DesJardin [54]) and computational parcels from **b** the present model, **c** Senda et al.'s model [63, 64], and **d** Bai and Gosman's model [49]. Reprinted under permission of John Wiley & Sons



The droplet surface energy and the work for a droplet to rebound are [60]:

$$E_{S,2} = \pi \alpha (1 - \alpha) D_{\max}^2 \sigma \left( \frac{\pi}{2} - \cos \theta_1 \right), \tag{19}$$

$$\frac{We_{rebound}}{E_{S,2}} = 0.35 \beta_{\max}^{0.56} (1 - \cos \theta_1)^{0.24}, \tag{20}$$

where  $\beta_{\max}$  is specified according to an empirical model for low-viscosity fluids [61].

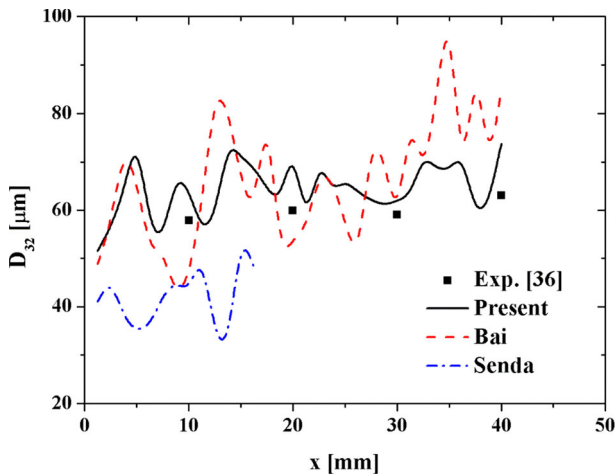
The surface-tension energy after rebounding (state 2) was assumed to be the same as the surface-tension energy before impingement (state 1):

$$E_{S,3} = E_{S,1} = \sigma \pi D_1^2, \tag{21}$$

Substituting Eqs. 19–21 into Eq. 18 yields the kinetic energy after rebounding and the rebounding droplet velocity.

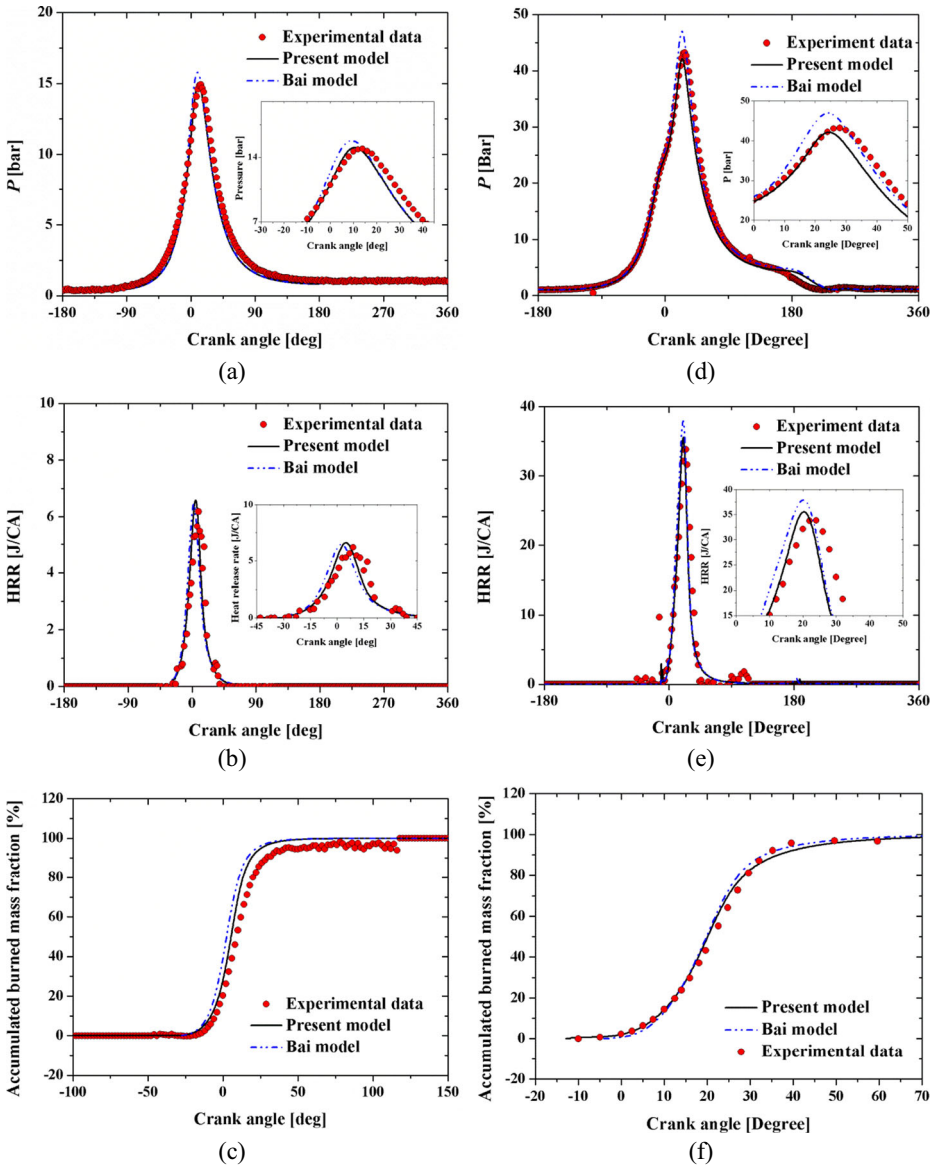
Figure 5 summarizes Weber number data for a rebounding isooctane droplet based on the study of Wachters and Westerling [62] and a simulation adopting the present model and Bai and Gosman’s model [49]. The  $x$  axis is the Weber number of the droplet before impingement,  $We_{in}$ , and the  $y$  axis is the Weber number after droplet impingement,  $We_{out}$ . These results were calculated from a CFD simulation using a  $0.2 \times 0.2 \times 0.2 \text{ m}^3$  ( $80 \times 80 \times 80$  grid) computational domain. The filled triangles are from the experiments of Wachters and Westerling [64], and the best-fit curve supplies the correlation used in this model. Our prediction (filled stars) showed similar trends to those of Wachters and Westerling for a rebounding isooctane droplet [62].

Figure 6 shows the experimental data and predicted spray impingement according to our model, Senda et al.’s model [63, 64], and Bai and Gosman’s model [49]. These results corresponded to the experimental data (Fig. 6a) obtained by Powell and Lee [65] and was reprinted in the study of Yoon and DesJardin [54]. The experimental image was taken at 10 ms, and the domain was  $52 \times 26 \text{ mm}^2$ . The injected liquid was isooctane. The results were compared in an identical  $80 \times 80 \times 80$  grid computational domain. The mass flow rate and injection period from the experimental data obtained by



**Fig. 7** Comparison between the measured SMD and three spray-impingement models where  $x$  is the distance from drop impact

Powell and Lee [65] were  $\dot{m} = 0.00144$  kg/s and 8.45 ms, respectively. Figure 7 shows the SMD or  $D_{32}$  from Fig. 6. The SMD results were taken along the radial distance ( $x$ -axis) from the impingement point, while the vertical distance was 5 mm above the



1500 rpm/BMEP 1.5 bar

2000 rpm/WOT (BMEP 10.5 bar)

**Fig. 8** Comparison between the experimental data and simulations under operating conditions of 1500 rpm/BMEP 1.5 bar: **a** pressure, **b** HRR, and **c** accumulated burned mass fraction. Comparison under operating conditions of 2000 rpm/WOT: **d** pressure, **e** HRR, and **f** accumulated burned mass fraction

impingement surface. The results showed that our model and Bai and Gosman’s model [49] both qualitatively matched the experimental data of Powell and Lee [65], while Senda et al.’s model [63, 64] underestimated the experimental data. The SMD increased with respect to the radial distance. Larger droplets had higher inertia and traveled further than small droplets.

### 4.2 Engine validation

After the spray impingement was characterized and modeled, experimental data were compared to numerical simulations performed under the operating conditions listed in Table 1.

Figure 8a–e compare the experimental data to simulated pressure, heat-release rate (HRR), and accumulated burned-mass fraction averaged over 50 cycles. Figure 8a–c show results when operating at 1500 rpm under a BMEP of 1.5 bar. Figure 8d–f show results when operating at 2000 rpm with a wide open throttle (WOT). The experimental data under each

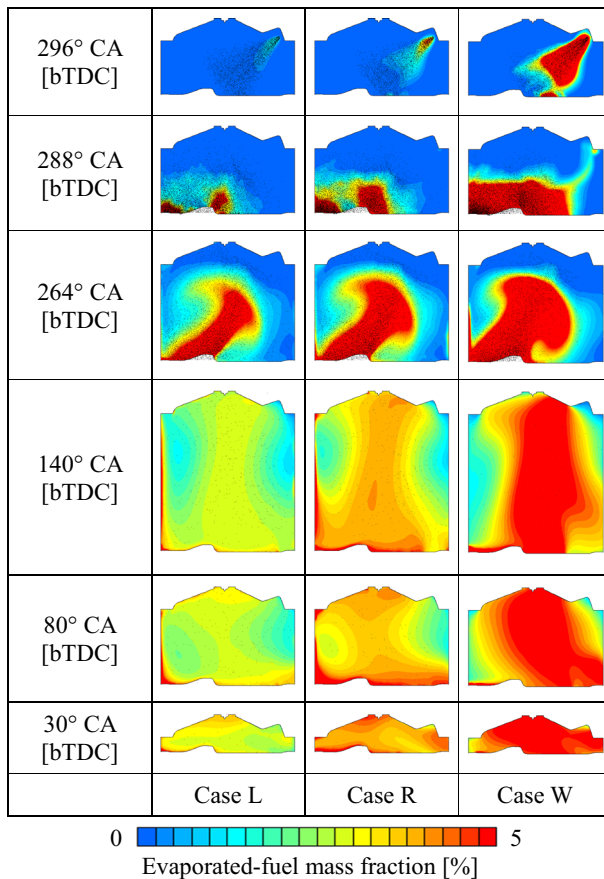


**Fig. 9** Evaporated-fuel mass fraction contours for each ambient-temperature case

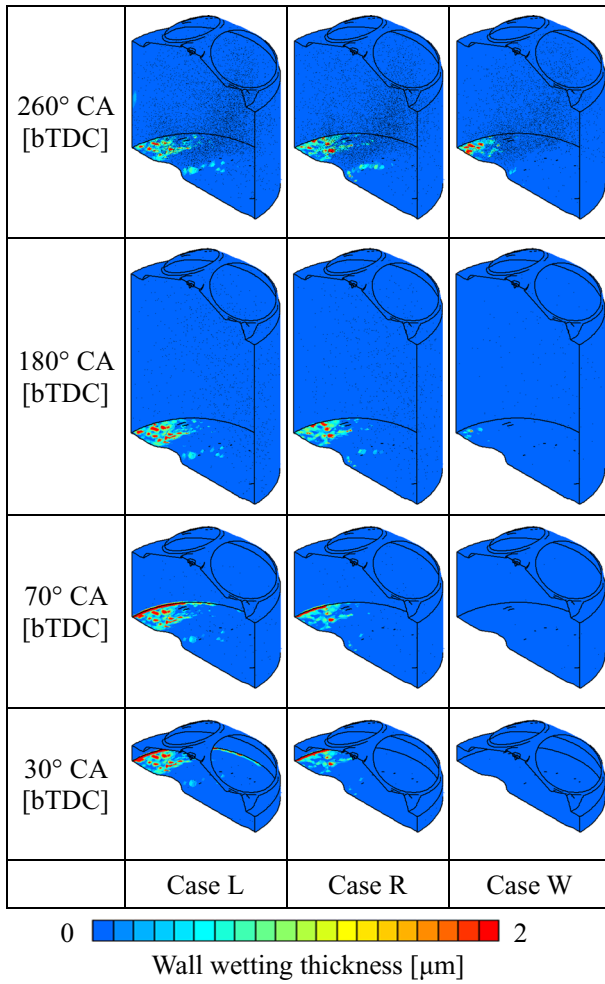


**Fig. 10** Wall-wetting thicknesses for each ambient temperature case

set of operating conditions were compared with the simulations from the present model and Bai and Gosman’s model [49]. Overall trends from each simulation matched the experimental data. However, the present model demonstrated improved accuracy across all results.

**Table 3** Fuel quantities for each ambient temperature Case R

Fuel quantities [%]	In-cylinder (Evaporated)	Intake port (Evaporated)	Wall-wetting
Case L	63.17	6.47	30.36
Case R	78.9	8.13	12.97
Case W	90.06	9.78	0.16

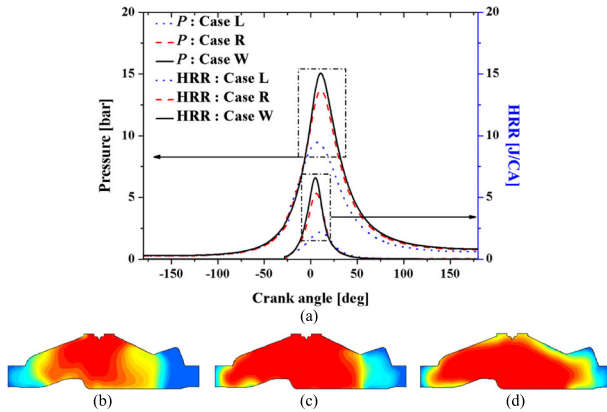


**Fig. 11** a Pressure and HRR histories. Burned-fuel mass fractions for b Case L, c Case R, and d Case W. The contours were at aTDC 30° CA for each case

The peak values from the Bai and Gosman model were slightly overestimated and the timing of the peak value was advanced. The present model simulated the peak pressure and HRR with deviations from measured values of only 1 % (3° CA) and 6.5 % (3.8° CA), respectively. On the other hand, the peak pressure and HRR from Bai and Gosman’s model showed deviations of 5.8 % (4.9° CA) and 4.3 % (6.6° CA), respectively. The numbers in parentheses are the deviation at the peak. Model error may be incurred because of variation in fuel distribution within the combustion chamber.

The experimental and simulated air masses at 1500 rpm/BMEP 1.5 bar were 70.6 and 75.1 mg/stroke, respectively. The simulated air mass was 6.4 % higher than the experimental air mass. Similarly, the experimental and simulated air masses at 2000 rpm/WOT were 296 and 305 mg/stroke, respectively, for a 3 % error. Differences from the experimental data could arise because the modeled intake pressure was based on an average measured value rather than the measured pressure trace, which varied in the experiment.

Note that the intake/exhaust pressure, SOI/EOI, and ignition time at 2000 rpm/WOT were 1.01/1.11 bar, 300°/262° CA bTDC, and 12.4° CA bTDC, respectively.

### 4.3 Effect of ambient temperature

Hereinafter, the wall and intake air temperatures are referred to as the ambient temperature. Three simulations were conducted with ambient temperatures of 273, 293, and 410 K: Cases L (low temperature), R (room temperature), and W (warmed-up temperature), respectively. The injection and spark timing were not changed.

**Table 4** Burned-fuel mass fractions engine, out NO and soot emission for each ambient temperature Case R

	Burned-fuel mass fraction [%]	Emission [g/kW-hr]	
		NO emission	Soot emission
Case L	60.82	0.28	3.1
Case R	83.07	1.65	1.13
Case W	85.38	5.39	0.0006

Figure 9 shows the behavior of the injected droplets (black dots in the top three rows of figures) and distribution of evaporated fuel at each ambient temperature. Droplet movements were similar in each case, but droplet evaporation was enhanced as the ambient temperature increased. Case L had the lowest evaporation rate, with most of the droplets surviving the intake and compression strokes. Most of the droplets were still present at ignition. In contrast, Case W showed the highest evaporation rate, which was evident even during fuel injection (see 296° CA bTDC of Case W).

Figure 10 shows wall-wetting distributions inside the combustion chamber for the three cases. As expected, wall wetting increased as the ambient temperature decreased. Most of the wall wetting occurred on the top of the piston, while the cylinder wall and combustion dome showed only minimal wetting. Although some cylinder-wall wetting was evident, thicknesses were minimal and thus are not evident in the figure. However, wall wetting accumulated at the contact between the cylinder wall and piston, especially late in the compression stroke. For Case W, only 0.2 % of the liquid fuel remained at the time of ignition; 99.8 % of the fuel evaporated under warmed-up conditions.

Table 3 lists the fuel quantities remaining at ignition time for each ambient-temperature case. The fuel quantities in the cylinder and intake port only represent the evaporated fuel because less than 1 % of the fuel remained in droplet form. As the ambient temperature decreased, the amount of wall wetting increased. In Case L, 30 % of the fuel wetted the

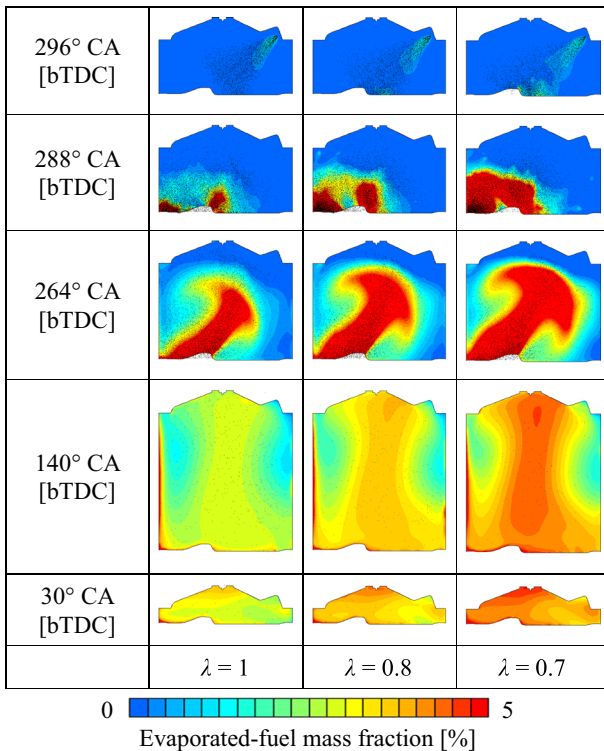


**Fig. 12** Evaporated-fuel mass fraction for variable  $\lambda$  (Case L)

walls at ignition. As more fuel evaporated with increasing ambient temperature, more fuel back-flowed into the intake port. Case W had 10 % of the total fuel mass back-flow into the intake port. Case L had the lowest back-flow at only 6.5 %.

Figure 11a shows the effect of decreasing the ambient temperature on the pressure, HRR, and burned-fuel mass fraction. Less evaporated fuel (Case L) resulted in lower pressures and HRR. The peak pressures of Cases L and R were 63 % and 91 % lower, respectively, than those of Case W. Case L had the lowest peak HRR value, and a lower HRR decreased the peak pressure. Note that peak HRR typically precedes peak pressure. However, the opposite tendency was observed here because that the flame speed was slower. Figure 11b–d show contours of the burned-fuel mass fraction, defined as the burned mass divided by the evaporated-fuel mass within the combustion chamber. The burned-fuel mass fraction represents how the combustion proceeded and is related to the flame propagation speed. The slower flame speed resulted in a slower combustion process, which led to heat being released over a longer duration. Slower flame speeds in Case L was due to the low mass of evaporated fuel, which yielded a lean mixture in the combustion chamber.

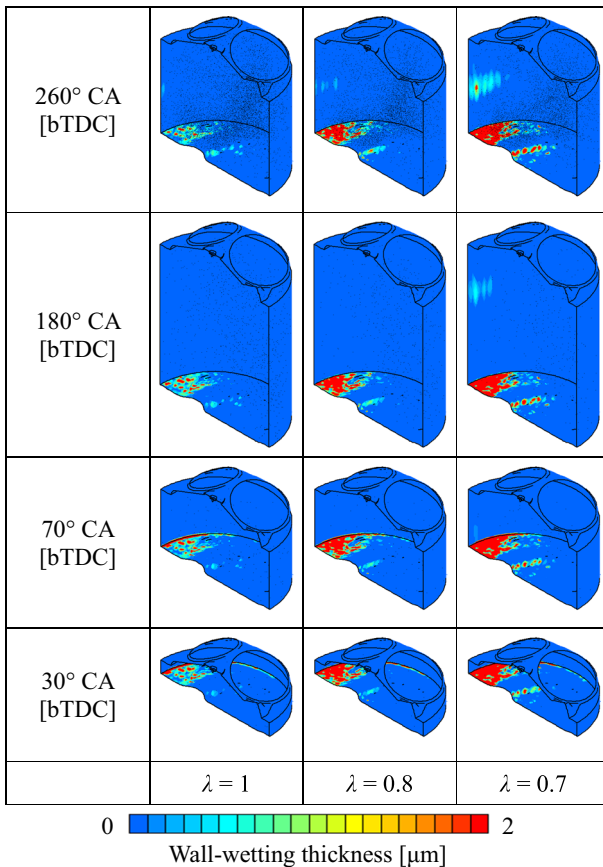


**Fig. 13** Wall-wetting distribution for variable  $\lambda$  (Case L)

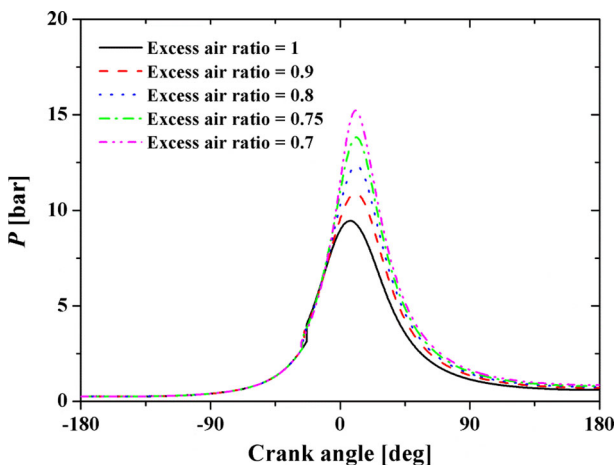
**Table 5** Fuel quantities for varied  $\lambda$  in units of mass and the portion of evaporated-fuel to the total fuel

	Fuel quantities [mg]			Fuel quantities [%]		
	In-cylinder	Intake port	Wall-wetting	In-cylinder	Intake port	Wall-wetting
$\lambda = 1$	3.19	0.33	1.53	63.17	6.47	30.36
$\lambda = 0.9$	3.52	0.37	1.7	62.90	6.65	30.44
$\lambda = 0.8$	3.73	0.41	1.9	61.75	6.72	31.53
$\lambda = 0.75$	3.96	0.44	2.13	60.62	6.74	32.64
$\lambda = 0.7$	4.27	0.47	2.36	60.16	6.67	33.17

Table 4 presents the final burned-fuel mass fractions, normalized emission indices for engine-out NO, and corresponding soot generation for each case. The burned-fuel mass fraction decreased with ambient temperature. For Case L, fuel consumption was only 61 %, which resulted in unstable combustion and low pressures. The fuel mass fraction burned in Cases R and W differed by only about 2 %. Unburned fuel increase soot mass. Because engine-out NO emissions increases significantly when the temperature exceeds 1800 K [66], Cases R and W showed significantly higher NO masses compared to Case L. However, Cases C and R generated significant soot masses, primarily from wall wetting. The engine-out soot mass for Cases L, R, and W were  $3.1$ ,  $1.13$ , and  $6.1 \times 10^{-4}$  g/kW-hr, respectively.

#### 4.4 Effect of excess air ratio

For Case L, the excess air ratio,  $\lambda$ , was varied from 0.7 to 0.8 to 1 to investigate its effect on wall wetting, pressure, and soot mass. The fuel-injection rate was increased to establish the excess air ratio, while the injection timing and duration were fixed.

**Fig. 14** Pressure histories for variable  $\lambda$  (Case L)

**Table 6** Burned-fuel mass fractions engine out NO and soot emission for varied  $\lambda$

	Burned-fuel mass fraction [%]	Emission [kg/kW-hr]	
		NO emission	Soot emission
$\lambda = 1$	60.82	0.28	3.1
$\lambda = 0.9$	73.73	0.48	3.12
$\lambda = 0.8$	78.81	0.84	3.15
$\lambda = 0.75$	82.36	1.52	3.5
$\lambda = 0.7$	84.14	2.67	3.79

Figure 12 shows the behavior of the injected droplets (black dots in the top three rows of figures) and the distribution of evaporated-fuel mass fraction for each excess air ratio. As more fuel was injected (increased  $\lambda$ ), more droplets impinged upon the piston top. As the intake stroke proceeded to BDC (from 360° CA bTDC to 180° CA bTDC), fuel droplets accumulated on the side of the cylinder and piston opposite the fuel injector. This led to increased wetness on the cylinder wall as  $\lambda$  decreased.

Figure 13 shows the wall-wetting distribution for decreasing  $\lambda$ . During injection, fuel droplets impinged and spread on the piston, similar to the results in Fig. 12. As  $\lambda$  decreased, the wetted wall area and thickness increased on the piston while also forming on the cylinder

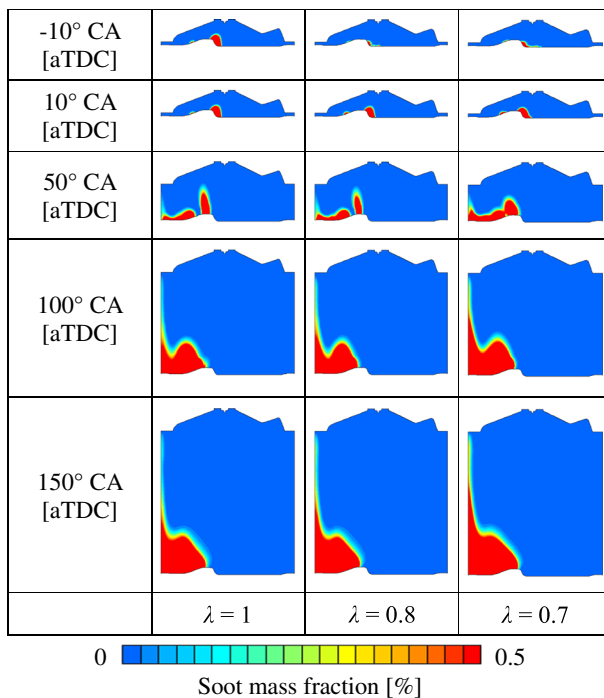


**Fig. 15** Soot mass fractions in combustion chamber for variable  $\lambda$  (Case L)

wall. The wetted thickness was greatest at the intersection between the piston head and cylinder wall. More droplets survived to ignition as  $\lambda$  decreased.

Table 5 lists the fuel quantity (mass and mass fraction) at ignition for each excess air ratio. As  $\lambda$  decreased, both the mass fraction of evaporated-fuel inside the combustion chamber and wall wetting increased. The evaporated fuel that back-flowed through the intake port was generally less than 0.47 mg. However, the evaporated-fuel mass and wall wetting increased while the portion of the evaporated-fuel to the total fuel decreased as  $\lambda$  decreased. For  $\lambda = 0.9$ , the mass fractions of the evaporated-fuel inside the combustion chamber and mass fraction of fuel wetting the wall were 62.9 % and 30.4 %, respectively. For  $\lambda = 0.7$ , these mass fractions were 60.2 % and 33.2 %, respectively.

Figure 14 shows the pressure during the compression and combustion strokes as a function of the crank angle. As  $\lambda$  decreased, the peak pressure increased. Table 6 lists the burned-fuel mass fractions during combustion; as  $\lambda$  decreased, the burned-fuel mass fraction increased. Moreover, decreased evaporated fuel decrease the peak pressure because less fuel was combusted. Note that the maximum temperature during combustion as  $\lambda$  increased ranged from 1330 to 1988 K, following the same trend as the pressure. The normalized engine-out NO emission indices and soot generation for various  $\lambda$  are listed in Table 6. The highest engine-out NO emissions were at  $\lambda = 0.7$  because temperatures exceeded 1800 K. These emissions were 9.6 times greater than those when  $\lambda = 1$ . Similarly, the soot generation for  $\lambda = 0.7$  was about 2.58 times higher than when  $\lambda = 1$ .

Figure 15 displays soot-generation contours for various  $\lambda$ . As  $\lambda$  decreased, the wet wall close to the cylinder yielded increased soot mass. For  $\lambda = 0.7$ , soot was predominantly generated along the wet wall near the piston top. Figures 13 and 15 show that the wall-wetting distribution and soot generation are correlated.

## 5 Conclusions

In this study, the spray impingement and combustion characteristics of a GDI engine under cold, room-temperature, and warmed-up driving conditions were simulated. For cold driving conditions,  $\lambda$  was also varied. To run accurate engine simulations, a spray impingement model was developed from experimental data and previous studies. Experimental data were used to verify the engine simulations. As the ambient temperature decreased, the wall wetting increased, which decreased pressure consequently yielding increased soot mass. The simulations revealed increased fuel consumption during combustion when  $\lambda$  was low (i.e., the rate of fuel mass injection was increased). This increased the in-cylinder pressure but also increased the wall-wetting mass, which resulted in increased soot generation.

**Acknowledgments** This work was supported by the Korea University Grant, Hyundai Motors Company, and Hyundai Next Generation Vehicle (NGV).

## References

1. Schwarz, C., Schünemann, E., Durst, B., Fischer, J., Witt, A.: Potentials of the spray-guided BMW DI combustion system. SAE Technical Paper 2006-01-1265 (2006)
2. Husted, H., Spegar, T.D., Spakowski, J.: The Effects of GDI Fuel Pressure on Fuel Economy: SAE Technical Paper 2014-01-1438 (2014)

3. Grimaldi, F., Gervais, D., Marchal, A., Floch, A.: Single-cylinder Experiments for Downsizing-Oriented SI Concepts: GDI and VVL Thermodynamic Comparison. SAE Technical Paper 2007-24-0013 (2007)
4. Weststrate, B., Warren, C., Vanderwege, B., Coulson, G., Anderson, R.: Dynamometer development results for a stratified-charge DISI combustion system. SAE Technical Paper 2002-01-2657 (2002)
5. Hoffmann, G., Befrui, B., Berndorfer, A., Piock, W.F., Varble, D.L.: Fuel system pressure increase for enhanced performance of GDI multi-hole injection systems. SAE Technical Paper 2014-01-1209 (2014)
6. Matsumoto, A., Moore, W.R., Lai, M.-C., Zheng, Y., Foster, M., Xie, X.-B., Yen, D., Confer, K., Hopkins, E.: Spray characterization of ethanol gasoline blends and comparison to a CFD model for a gasoline direct injector. SAE Technical Paper 2010-01-0601 (2010)
7. Stojkovic, B.D., Fansler, T.D., Drake, M.C., Sick, V.: High-speed imaging of OH\* and soot temperature and concentration in a stratified-charge direct-injection gasoline engine. Proc. Combust. Inst. **30**(2), 2657–2665 (2005)
8. Stevens, E., Steeper, R.: Piston wetting in an optical DISI engine: fuel films, pool fires, and soot generation. SAE Technical Paper 2001-01-1203 (2001)
9. Sabathil, D., Koenigstein, A., Schaffner, P., Fritzsche, J., Doehler, A.: The influence of DISI engine operating parameters on particle number emissions. SAE Technical Paper 2011-01-0143 (2011)
10. Desoutter, G., Cuenot, B., Habchi, C., Poinso, T.: Interaction of a premixed flame with a liquid fuel film on a wall. Proc. Combust. Inst. **30**(1), 259–266 (2005)
11. Drake, M.C., Fansler, T.D., Solomon, A.S., Szekely, G.: Piston fuel films as a source of smoke and hydrocarbon emissions from a wall-controlled spark-ignited direct-injection engine. 0096-736X, SAE Technical Paper 2003-01-0547 (2003)
12. Choi, K., Kim, J., Ko, A., Myung, C.-L., Park, S., Lee, J.: Size-resolved engine exhaust aerosol characteristics in a metal foam particulate filter for GDI light-duty vehicle. J. Aerosol. Sci. **57**, 1–13 (2013)
13. Piock, W., Hoffmann, G., Berndorfer, A., Salemi, P., Fusshoeller, B.: Strategies towards meeting future particulate matter emission requirements in homogeneous gasoline direct injection engines. SAE Technical Paper 2011-01-1212 (2011)
14. Whitaker, P., Kapus, P., Ogris, M., Hollerer, P.: Measures to reduce particulate emissions from gasoline DI engines. SAE Technical Paper 2011-01-1219 (2011)
15. Seo, J., Lee, J.S., Choi, K.H., Kim, H.Y., Yoon, S.S.: Numerical investigation of the combustion characteristics and wall impingement with dependence on split-injection strategies from a gasoline direct-injection spark ignition engine. Proc. Inst. Mech. Eng. Part D: J. Automobile Eng. **227**(11), 1518–1535 (2013)
16. Li, T., Nishida, K., Zhang, Y., Yamakawa, M., Hiroyasu, H.: An insight into effect of split injection on mixture formation and combustion of DI gasoline engines. SAE Technical Paper 2004-01-1949 (2004)
17. Fan, Q., Li, L., Hu, Z., Deng, J.: Spray Characteristics and Wall-impingement Process with Different Piston Tops for the Multi-hole Injector of DISI Gasoline Engines. SAE Technical Paper 2011-01-1222 (2011)
18. Ristimäki, J., Keskinen, J., Virtanen, A., Maricq, M., Aakko, P.: Cold temperature PM emissions measurement: Method evaluation and application to light duty vehicles. Environ. Sci. Technol. **39**(24), 9424–9430 (2005)
19. Serras-Pereira, J., Aleiferis, P.G., Richardson, D.: Imaging and heat flux measurements of wall impinging sprays of hydrocarbons and alcohols in a direct-injection spark-ignition engine. Fuel **91**(1), 264–297 (2012)
20. Park, S., Ghandhi, J.: Fuel film temperature and thickness measurements on the piston crown of a direct-injection spark-ignition engine. SAE Technical Paper 2005-01-0649 (2005)
21. O'Rourke, P.J.: A spray/wall interaction submodel for the KIVA-3 wall film model. SAE Technical Paper 2000-01-0271 (2000)
22. Yi, J., Han, Z., Xu, Z., Stanley, L.E.: Combustion improvement of a light stratified-charge direct injection engine. 0096-736X, SAE Technical Paper 2004-01-0546 (2004)
23. Millo, F., Badami, M., Bianco, A., Delogu, E.: CFD diagnostic methodology for the assessment of mixture formation quality in GDI engines. SAE Technical Paper 2011-24-0151 (2011)
24. STAR-CD Version 4.20 User Manual and Methodology
25. Issa, R.I.: Solution of the implicitly discretised fluid flow equations by operator-splitting. J. Computat. Phys. **62**(1), 40–65 (1986)
26. Asproulis, P.: High resolution numerical predictions of hypersonic flows on unstructured meshes. Ph.D Thesis. Imperial College London (1994)
27. Kuo, K.K.K.: Principles of Combustion, 1st Edn. Wiley (1986)

28. El Wakil, M.M., Ueyehara, O., Myers, P.: A theoretical investigation of the heating-up period of injected fuel droplets vaporizing in air. NACA Technical Note, 3179 (1954)
29. Bai, C.: Modelling of spray impingement processes. SAE Technical Paper 960626 (1996)
30. Torres, D., O'Rourke, P., Amsden, A.: Efficient multicomponent fuel algorithm. *Combustion Theory and Modelling* **7**(1), 67–86 (2003)
31. Friedrich, M.A., Lan, H., Wegener, J., Drallmeier, J., Armaly, B.F.: A separation criterion with experimental validation for shear-driven films in separated flows. *J. Fluids Eng.* **130**(5), 051301 (2008)
32. Maroteaux, F., Llory, D., Le Coz, J., Habchi, C.: Liquid film atomization on wall edges—separation criterion and droplets formation model. *J. Fluids Eng.* **124**(3), 565–575 (2002)
33. Yakhot, V., Orszag, S., Thangam, S., Gatski, T., Speziale, C.: Development of turbulence models for shear flows by a double expansion technique. *Phys. Fluids A: Fluid Dyn.* **4**(7), 1510–1520 (1992)
34. Reitz, R.D., Diwakar, R.: Effect of drop breakup on fuel sprays. SAE Technical Paper 860469 (1986)
35. O'Rourke, P.J.: Collective drop effects on vaporizing liquid sprays. Ph.D Thesis. Princeton University (1981)
36. Colin, O., Benkenida, A.: The 3-Zones Extended Coherent Flame Model (Ecfm3z) for Computing Premixed/Diffusion Combustion Le modèle ECFM3Z (3-Zones Extended Coherent Flame Model) pour le calcul de la combustion par flammes de prémélange et flammes de diffusion. *Oil Gas Sci. Technol.* **59**, 593–609 (2004)
37. Colin, O., Benkenida, A., Angelberger, C.: 3D modeling of mixing, ignition and combustion phenomena in highly stratified gasoline engines. *Oil Gas Sci. Technol.* **58**(1), 47–62 (2003)
38. Metghalchi, M., Keck, J.C.: Burning velocities of mixtures of air with methanol, isooctane, and indolene at high pressure and temperature. *Combust. Flame* **48**, 191–210 (1982)
39. Meneveau, C., Poinso, T.: Stretching and quenching of flamelets in premixed turbulent combustion. *Combustion and Flame* **86**(4), 311–332 (1991)
40. Fichot, F., Lacas, F., Veynante, D., Candel, S.: One-dimensional propagation of a premixed turbulent flame with a balance equation for the flame surface density. *Combust. Sci. Technol.* **90**(1–4), 35–60 (1993)
41. Karlsson, A., Magnusson, I., Balthasar, M., Mauss, F.: Simulation of soot formation under diesel engine conditions using a detailed kinetic soot model. SAE Technical Paper 981022 (1998)
42. Han, Z., Yi, J., Trigui, N.: Stratified mixture formation and piston surface wetting in a DISI engine. SAE Technical Paper 2002-01-2655 (2002)
43. Drake, M.C., Haworth, D.C.: Advanced gasoline engine development using optical diagnostics and numerical modeling. *Proc. Combust. Inst.* **31**(1), 99–124 (2007)
44. Chryssakis, C., Assanis, D.N.: A unified fuel spray breakup model for internal combustion engine applications. *Atomization and Sprays* **18**(5) (2008)
45. Mundo, C., Sommerfeld, M., Tropea, C.: Droplet-wall collisions: Experimental studies of the deformation and breakup process. *Int. J. Multiphase Flow* **21**(2), 151–173 (1995)
46. Rosa, N.G., Villedieu, P., Dewitte, J., Lavergne, G.: A new droplet-wall interaction model. In: Proceedings of the 10th International Conference on Liquid Atomization and Spray System, Tokyo (2006)
47. Stanton, D.W., Rutland, C.J.: Modeling fuel film formation and wall interaction in diesel engines. SAE Technical Paper 960628 (1996)
48. Grover, R.O., Assanis, D.N.: A spray wall impingement model based upon conservation principles. In: 5th International Symposium on Diagnostics and Modeling of Combustion in Internal Combustion Engines, Nagoya (2001)
49. Bai, C., Gosman, A.: Development of methodology for spray impingement simulation. SAE Technical Paper 950283 (1995)
50. Yarin, A., Weiss, D.: Impact of drops on solid surfaces: self-similar capillary waves, and splashing as a new type of kinematic discontinuity. *J. Fluid Mech.* **283**, 141–173 (1995)
51. Stow, C., Stainer, R.: The physical products of a splashing water drop. *J. Meteorolog. Soc. Jpn.* **55**, 518–532 (1977)
52. Mutchler, C.K.: Size, travel and composition of droplets formed by waterdrop splash on thin water layers. Ph.D Thesis, University of Minnesota (1970)
53. Marmanis, H., Thoroddsen, S.: Scaling of the fingering pattern of an impacting drop. *Phys. Fluids* **8**(6), 1344–1346 (1996)
54. Yoon, S.S., DesJardin, P.E.: Modelling spray impingement using linear stability theories for droplet shattering. *Int. J. Numer. Methods Fluids* **50**(4), 469–489 (2006)
55. McCarthy, M., Molloy, N.: Review of stability of liquid jets and the influence of nozzle design. *Chem. Eng. J.* **7**(1), 1–20 (1974)
56. Weber, C.: Zum zerfall eines flüssigkeitsstrahles. *Z. Angew. Math. Mech.* **11**(2), 136–154 (1931)

57. Allen, R.F.: The role of surface tension in splashing. *J. Colloid Interface Sci.* **51**(2), 350–351 (1975)
58. Ghadiri-Khorzooghi, H.: Raindrop Impact, Soil Splash, and Cratering. Ph.D Thesis, University of Reading (1978)
59. Montanaro, A., Malaguti, S., Alfuso, S.: Wall impingement process of a multi-hole GDI spray: Experimental and numerical investigation. SAE Technical Paper 2012-01-1266 (2012)
60. Ryu, S.: An experimental study on post-impingement behavior of an electrically charged droplet. Ph.D Thesis, Korea Advanced Institute of Science and Technology (2008)
61. Seo, J., Lee, J.S., Kim, H.Y., Yoon, S.S.: Empirical model for the maximum spreading diameter of low-viscosity droplets on a dry wall. *Exp. Therm Fluid Sci.* **61**, 121–129 (2015)
62. Wachters, L., Westerling, N.: The heat transfer from a hot wall to impinging water drops in the spheroidal state. *Chem. Eng. Sci.* **21**(11), 1047–1056 (1966)
63. Senda, J., Kanda, T., Al-Roub, M., Farrell, P.V., Fukami, T., Fujimoto, H.: Modeling spray impingement considering fuel film formation on the wall. SAE Technical Paper 970047 (1997)
64. Senda, J., Kobayashi, M., Iwashita, S., Fujimoto, H.: Modeling of diesel spray impinging on flat wall. SAE Technical Paper 941894 (1994)
65. Powell, J., Lee, C.F.: Experimental top and side view pictures of an impinging fuel spray, Madison (2002)
66. Christensen, M., Johansson, B., Amnéus, P., Mauss, F.: Supercharged homogeneous charge compression ignition. SAE Technical Paper 980787 (1998)